Detectors for the James Webb Space Telescope Near-Infrared Spectrograph I: Readout Mode, Noise Model, and Calibration Considerations

Bernard J. Rauscher and Ori Fox[1]

NASA Goddard Space Flight Center, Greenbelt, MD 20771

Bernard.J.Rauscher@nasa.gov

Pierre Ferruit[2,3]

Université de Lyon, Lyon, F-69003, France

Robert J. Hill[8], Augustyn Waczynski[4], Yiting Wen[6], Wei Xia-Serafino[4], Brent Mott,

David Alexander, Clifford K. Brambora, Rebecca Derro, Chuck Engler,

Matthew B. Garrison, Thomas Johnson, Sridhar S. Manthripragada, James M. Marsh,

Cheryl Marshall, Robert J. Martineau, Kamdin B. Shakoorzadeh[7], Donna Wilson,

Wayne D. Roher[5], and Miles Smith

NASA Goddard Space Flight Center, Greenbelt, MD 20771

Craig Cabelli, James Garnett, Markus Loose,

Selmer Wong-Anglin, Majid Zandian, and Edward Cheng[8]

Teledyne Imaging Sensors, 5212 Verdugo Way, Camarillo, CA 93012

Timothy Ellis, Bryan Howe, Miriam Jurado,

Ginn Lee, John Nieznanski, Peter Wallis, and James York

ITT Space Systems Division, 1447 St. Paul Street, Rochester, NY, 14653

Michael W. Regan

Space Telescope Science Institute, 3700 San Martin Drive, Baltimore, MD 21218

Donald N.B. Hall and Klaus W. Hodapp

Institute for Astronomy, 640 North Aóhoku Place, #209, Hilo HI 96720

and

Torsten Böker, Guido De Marchi, Peter Jakobsen, and Paolo Strada

ESTEC, Astrophysics Division, Postbus 299, Noordwijk, NL2200 AG, Netherlands

[1]Also at Department of Astronomy, University of Virginia, P.O. Box 4000325, Charlottesville, VA 22904

[2]Also at Université Lyon 1, Observatoire de Lyon, 9 avenue Charles André, Saint-Genis Laval, F-69230, France

[3]Also at CNRS, UMR 5574, Centre de Recherche Astrophysique de Lyon; Ecole Normale Supérieure de Lyon, Lyon, F-69007, France

[4]Global Science & Technologies, Inc., 7855 Walker Drive, Suite 200, Greenbelt, MD 20770

[5]Northrop Grumman Technical Services, 4276 Forbes Blvd., Lanham, MD 20706

[6]Muniz Engineering Inc., 7404 Executive Place, Suite 500, Lanham, MD 20706

[7]AK Aerospace Technology Corp., 12970 Brighton Dam Rd, Clarksville, MD 21029

[8]Conceptual Analytics LLC, 8209 Woburn Abbey Road, Glenn Dale, MD 20769

ABSTRACT

We describe how the James Webb Space Telescope (JWST) Near-Infrared Spectrograph's (NIRSpec's) detectors will be read out, and present a model of how noise scales with the number of multiple non-destructive reads sampling-up-the-ramp. We believe that this noise model, which is validated using real and simulated test data, is applicable to most astronomical near-infrared instruments. We describe some non-ideal behaviors that have been observed in engineering grade NIRSpec detectors, and demonstrate that they are unlikely to affect NIRSpec sensitivity, operations, or calibration. These include a HAWAII-2RG reset anomaly and random telegraph noise (RTN). Using real test data, we show that the reset anomaly is: (1) very nearly noiseless and (2) can be easily calibrated out. Likewise, we show that large-amplitude RTN affects only a small and fixed population of pixels. It can therefore be tracked using standard pixel operability maps.

Subject headings: Astronomical Instrumentation

1. Introduction

The James Webb Space Telescope (JWST) was conceived as the scientific successor to NASA's Hubble and Spitzer space telescopes. Of all JWST "near-infrared" (NIR; $\lambda = 0.6 - 5\,\mu m$) instruments, the Near-Infrared Spectrograph (NIRSpec) has the most challenging detector requirements. This paper describes how we plan to operate NIRSpec's two 2048×2048 pixel, 5 micron cutoff (λ_{co}=5μm), Teledyne HAWAII-2RG (H2RG) sensor chip assemblies (SCAs)[1] for the most sensitive observations, and provides insights into some non-ideal behaviors that have been observed in engineering grade NIRSpec detectors.

This paper is structured as follows. In Section 2, we provide an introduction to JWST, NIRSpec, and NIRSpec's detectors. We have tried to keep this discussion brief, and provide references to more comprehensive discussions in the literature.

In Section 3, we present the NIRSpec detector subsystem's baseline MULTIACCUM readout mode. This section includes a detailed discussion of how total noise averages down when multiple non-destructive reads are used sampling-up-the-ramp. MULTIACCUM readout is quite general, and most other common readout modes, including correlated double sampling (CDS), multiple-CDS (MCDS; also known as Fowler-N; Fowler & Gatley 1991), and straight sampling-up-the-ramp are special cases of MULTIACCUM. The general NIR SCA noise model presented in this section, see Equation 1 & Table 2, is validated using real and simulated test data.

Where practical, our methods and conclusions are anchored by measurement. One advantage of the NIRSpec program is that multiple test SCAs and test facilities are

---

[1]Within NASA, individually mounted detector arrays are typically referred to as SCAs. In the case of NIRSpec's H2RGs, the SCA consists of HgCdTe detectors hybridized to a readout integrated circuit and mounted on a molybdenum base (See Figure 1).

available. These are described in Section 4.

Section 5 describes the reset anomaly as it appears in engineering grade NIRSpec H2RGs. The reset anomaly is fairly well-known in the NIR detector testing community. Here we demonstrate using real test data that it is a nearly noise-less artifact for the NIRSpec detectors that have been tested so far. We show that it straightforwardly calibrates out from most science observations, and can therefore be safely ignored by most JWST users. However, we show that the reset anomaly can significantly bias dark current measurements if it is not correctly accounted for. In this paper, we describe a method of accounting for the reset anomaly in dark current measurements by fitting a 4-parameter function to sampled-up-the-ramp pixels.

Finally, in Section 6, we describe what is known about random telegraph noise (RTN) within the NIRSpec program. Using real test data, we show that large-amplitude RTN is a property of only a small and fixed population of pixels for the SCAs that have been studied.[2] Based on these data, we do not expect RTN to significantly impact NIRSpec. While this conclusion may appear to render studies of RTN an academic exercise, it actually mitigates that risk that RTN could have a major impact if the affected pixels were to change from integration to integration.

Although our discussion is focused on JWST's NIRSpec, we anticipate that much of

----

[2]It is helpful to differentiate between large-amplitude RTN, that would probably cause a pixel to fail to meet total noise requirements, and the harder-to-find (but still important) small-amplitude RTN (near the read noise floor of the SCA) that was included in a study by Bacon et al. (2005). Unless otherwise indicated, we use the acronym RTN to refer to noise that significantly exceeds the read noise floor of the SCA. These points are discussed more fully in Section 6.

what we discuss will be of interest to any astronomer using H2RGs. The noise model is quite general, and we are aware of others having observed both the reset anomaly and RTN. However, one caveat is in order. Integration and testing of the NIRSpec detector subsystem is just beginning now. As such, we anticipate that much remains to be learned about NIRSpec's detectors, and that some of the specifics presented here may change. For this reason, we have tried to focus on general themes, rather than on the measured performance of any particular SCA.

2. JWST, NIRSpec, and the NIRSpec Detector Subsystem

2.1. JWST Mission

JWST is a large, cold, infrared-optimized space telescope designed to enable fundamental breakthroughs in our understanding of the formation and evolution of galaxies, stars, and planetary systems. The project is led by the United States National Aeronautics and Space Administration (NASA), with major contributions from the European and Canadian Space Agencies (ESA and CSA respectively). JWST will have an approximately 6.6-m diameter aperture, be passively cooled to below T=50 K, and carry four scientific instruments: NIRSpec, a NIR Camera (NIRCam), a NIR Tunable Filter Imager (TFI), and a Mid-Infrared Instrument (MIRI). All four scientific instruments are located in the Integrated Science Instruments Module (ISIM), which lies in the focal plane behind the primary mirror. JWST is planned for launch early in the next decade on an Ariane 5 rocket to a deep space orbit around the Sun-Earth Lagrange point L2, about 1.5×10^6 km from Earth. The spacecraft will carry enough fuel for a 10-year mission.

JWST's scientific objectives fall into four broad themes. These are as follows; (1) The End of the Dark Ages, First Light and Re-ionization, (2) The Assembly of Galaxies, (3)

The Birth of Stars and Protoplanetary Systems, and (4) Planetary Systems and the Origins of Life. Most NIR programs will require long, staring observations, limited by the zodiacal background at L2 in the case of NIRCam and the TFI, or by detector noise in the case of NIRSpec. For all of JWST's NIR instruments, modest $\approx$100-200 kHz pixel rates will be the rule, with total observing times per target typically $> 10^4$ seconds. Teledyne H2RGs have been selected as the detectors for all three JWST NIR instruments. For a more thorough overview of JWST, we refer the interested reader to Gardner (2006).

2.2. NIRSpec

NIRSpec will be the first slit-based astronomical multi-object spectrograph (MOS) to fly in space, and is designed to provide NIR spectra of faint objects at spectral resolutions of R=100, R=1000 and R=2700. The instrument's all-reflective wide-field optics, together with its novel MEMS-based programmable micro-shutter array slit selection device and H2RG detector arrays, combine to allow simultaneous observations of >100 objects within a 3.5×3.4 arcmin field of view with unprecedented sensitivity. A selectable 3×3 arcsec Integral Field Unit (IFU) and five fixed slits are also available for detailed spectroscopic studies of single objects. NIRSpec is presently expected to be capable of reaching a continuum flux of 20 nJy (AB>28) in R=100 mode, and a line flux of 6×10^{-19} erg s^{-1} cm^{-2} in R=1000 mode at S/N>3 in 10^4 s.

NIRSpec is being built for the European Space Agency (ESA) by EADS Astrium as part of ESA's contribution to the JWST mission. The NIRSpec micro-shutter and detector arrays are provided by NASA Goddard Space Flight Center (GSFC).

2.2.1. NIRSpec Detector Subsystem

All three NIRSpec modes (MOS, IFU and fixed slits) share the need for large-format, high detective quantum efficiency (DQE), and ultra-low noise detectors covering the $\lambda = 0.6 - 5\,\mu$m spectral range (see Table 1). This need is fulfilled by two $\lambda_{co} \sim 5\,\mu$m H2RG SCAs. These SCAs, and the two Teledyne SIDECAR[3] application specific integrated circuits (ASICs) that will control them, represent today's state-of-the-art. This hardware is being delivered to the European Space Agency (ESA) by the NIRSpec Detector Subsystem (DS) team at GSFC. The DS team will deliver a fully integrated, tested, and characterized DS to ESA for integration into NIRSpec.

The SIDECAR ASIC and NIRSpec SCA, and indeed all JWST SCAs, recently passed a major NASA milestone by achieving Technology Readiness Level 6 (TRL-6). TRL-6 is a major milestone in the context of a NASA flight program because it essentially marks the retirement of invention risk.

The DS (Figure 1) consists of the following components; focal plane assembly (FPA), two SIDECAR ASICs, focal plane electronics (FPE), thermal and electrical harnesses, and software. The molybdenum FPA is being built by Teledyne and their partner ITT. The two H2RG SCAs, which are the focus of this paper, are being built by Teledyne.

The SCA, Figure 1, was designed by Teledyne and ITT. Starting from the anti-reflection (AR) coating and going in, SCA components include; (1) AR coating, (2) 2K×2K HgCdTe pixel array, (3) silicon readout integrated circuit (ROIC), (4) balanced composite structure (BCS), (5) molybdenum base, (6) Rigidflex fanout circuit, and (7) μD-37 connector. Components 1-4 are built by Teledyne and components 5-7 are provided by ITT.

Although NIRSpec's DQE requirement is for $\lambda = 0.6 - 5\,\mu$m, the HgCdTe is actually

---

[3]SIDECAR: System for Image Digitization, Enhancement, Control and Retrieval.

being grown with a somewhat longer cutoff wavelength near to $\lambda_{co} \sim 5.3$ μm. This is done to ensure meeting the 80% DQE requirement at λ=5 μm, and is accomplished by varying the mole fraction of cadmium in the $Hg_{1-x}Cd_xTe$. In practice, proportionally less cadmium is used to achieve longer cutoffs (Brice 1987).

The H2RG ROIC and SIDECAR ASIC are both reconfigurable in software. For example, both can accommodate up to 32 video channels. For NIRSpec, however, we plan to use only four SCA analog outputs. This is driven by power dissipation considerations on-orbit, and by the need to minimize system complexity. Each NIRSpec detector will return 2048×2048 pixels of 16-bit data per frame. These will appear as a contiguous area of 2040×2040 photo-sensitive pixels, surrounded by a 4-pixels wide border of non-photo-sensitive reference pixels all the way around. Although the reference pixels do not respond to light, they have been designed to electrically mimic regular pixels. Previous testing has shown them to be highly effective at removing low frequency drifts like the "pedestal effect" which is familiar to HST NICMOS users (Arendt, Fixsen, & Moseley 2002).

In NIRSpec, the four outputs per SCA will appear as thick, 512×2048 pixels bands aligned with the dispersion direction. This is done to minimize the possibility of calibration difficulties in spectra that would otherwise span multiple outputs. Raw data will be averaged in the on-board focal plane array processor (FPAP) before being saved to the solid state recorder, and ultimately downlinked to the ground. The FPAP is located in the shared integrated command and data handling system (ICDH), and is not part of the DS. Averaging is done to conserve bandwidth for the data link to the ground. Following averaging, the data are still sampled-up-the-ramp, however each up-the-ramp data point has lower noise and the ramp is more sparsely sampled. Detector readout will be discussed in detail in Section 3.

Before turning to detector readout modes, it is appropriate to comment on the

performance of some prototype and engineering grade SCAs that have been built so far. In some cases, most notably prototype JWST SCAs H2RG-015-5.0μm and H2RG-006-5.0μm, the parts met demanding performance requirements including total noise per pixel, σ_{total} <6 e^- rms per 10^3 seconds integration and mean dark current, i_{dark} $\leq$0.010 e^- s^{-1} pixel^{-1}. Even with such outstanding detectors however, getting the most out of NIRSpec will require understanding both the ideal and non-ideal detector behaviors.

3. Detector Readout Modes

For most science observations, NIRSpec's detectors will acquire sampled-up-the-ramp data at a constant cadence of one frame every $\approx$10.5 s. A frame is the unit of data that results from sequentially clocking through and reading out a rectangular area of pixels. Most often, this will be all of the pixels in the SCA, although smaller sub-arrays are also possible when faster cadences are needed to observe e.g. bright targets. Although each of JWST's NIR instruments differs somewhat in the precise details, Figure 2 shows the JWST NIR detector readout scheme.

Following in the footsteps of NICMOS, we have dubbed this readout pattern MULTIACCUM. We frequently use the abbreviation MULTI-$n \times m$, where n is the number of equally spaced groups sampling-up-the-ramp and m is the number of averaged frames per group. For example, in Figure 2, n=6 and m=4. If a NIRSpec user were to see a raw H2RG FITS file, it would have dimensionality 2048$\times$2048$\times n$. Each group, in turn, is the result of averaging m 2048$\times$2048 pixel frames.

One advantage of sampled-up-the-ramp data for space platforms is that cosmic rays can potentially be rejected with minimal data loss. Briefly stated, we anticipate that cosmic ray hits will appear as discontinuous steps in pixel ramps. These steps can be identified,

and samples on either side of the hit can be used to recover the slope. This has previously been done for the HST NICMOS instrument, and we are studying it for NIRSpec now.

In the JWST usage, the integration time, t_{int}, is the time between digitizing pixel [0,0] in the first frame of the first group, and digitizing the same pixel in the first frame of the last group. The small overhead associated with finishing the last group is not included in the integration time.

Other important time intervals include the frame time, t_f, and the group time, t_g. The frame time is the time interval between reading pixel [0,0] in one frame, and reading the same pixel in the next frame within the same group. The group time is the time interval between reading pixel [0,0] in the first frame of one group, and reading the same pixel in the first frame of the next group. For NIRSpec, the integration time is related to the group time as follows, $t_{\mathrm{int}} = (n - 1)\, t_g$.

3.1. Importance of Matching Darks/Skys

For most astronomical NIR array detectors, it is good practice to use a highly redundant observing strategy and matching dark/sky integrations. A redundant observing strategy is one that samples each point on the sky or spectrum using more than one pixel. This is usually accomplished by building observations up from multiple, dithered integrations. The advantage of this practice is that the non-ideal behavior of particular pixels tends to average out, or can be identified using statistical tools during image stacking.

Matching darks and skys are dark or sky integrations that are taken using exactly the same readout mode as was used to obtain the science data. For example, if the science integrations use MULTI-22×4 readout, so should the darks. The same logic applies to imaging observations of the sky. The advantage of matching calibration data is that

artifacts such as residual bias (one manifestation of the reset anomaly, Section 5) subtract out.

For flight operations, one advantage of the MULTIACCUM readout pattern is that matching darks can be easily made for all integration times if darks are taken for the longest planned integration time. For example, if it is known that observers will use MULTI-22×4, MULTI-6×4, and MULTI-66×4 integrations, a set of MULTI-66×4 darks is all that is needed for the calibration pipeline. Darks for the shorter integration times can be made using only the first 22 and 6 averaged groups, respectively, from the MULTI-66×4 darks.

3.2. Modeling MULTIACCUM Sampled Data

In this section, we show that a general expression for the total noise variance of an electronically shuttered instrument using MULTIACCUM readout is,

$$\sigma_{\text{total}}^2 = \frac{12(n-1)}{mn(n+1)}\sigma_{\text{read}}^2 + \frac{6(n^2+1)}{5n(n+1)}(n-1)t_g f - \frac{2(2m-1)(n-1)}{mn(n+1)}(m-1)t_f f. \quad (1)$$

In this expression, σ_{total} is the total noise in units of e^- rms, σ_{read} is the read noise per frame in units of e^- rms, and f is flux in units of e^- s^{-1} pixel^{-1}, where f includes photonic current and dark current. The noise model includes read noise and shot noise on integrated flux, which is correlated across the multiple non-destructive reads sampling-up-the-ramp. For the special case of dark integrations, $f = i_{\text{dark}}$.

Equation 1 can also be used to model CDS and MCDS readout modes because both are special cases of MULTIACCUM. Table 2 summarizes the parameters to use for some common readout schemes. Under ultra-low photon flux and ultra-low dark current conditions, $\sigma_{\text{CDS}} \approx \sqrt{2}\sigma_{\text{read}}$.

An electronically shuttered instrument is one which does not use an opaque shutter to block light from the detectors in normal scientific operations. The main exception to

this rule is for taking dark integrations. This readout technique is in widespread use for space-based astronomical missions, and at ground-based observatories around the world. In an electronically shuttered instrument, the length of an integration is set by the readout pattern, and each pixel sees constant flux during an integration.

JWST testing has demonstrated that dark-subtracted MULTI-$n \times m$ sampled data for a pixel, (x,y), are usually well-modeled by a 2-parameter least-squares line fit of the form,

$$s_{x,y} = a_{x,y} + b_{x,y}t, \tag{2}$$

where $s_{x,y}$ is the integrating signal in units of e^-, $a_{x,y}$ is the y-intercept, $b_{x,y}$ is the slope, and t is time.[4] This point will be elaborated on in Section 5. One widely-available implementation is provided by IDL's LINFIT procedure. In practice, however, we have found that it is much more computationally efficient in IDL to work with full 2048×2048 pixel groups of data in parallel, and we compute the standard sums for least squares line fitting ourselves. On our Linux and OS X computers, computing the sums directly and in parallel is about 40× faster than calling LINFIT sequentially for every pixel in the cube! Moreover the demands on random access memory are greatly reduced because it is only necessary to

---

[4]For example 73% of dark subtracted pixels in engineering grade H2RG-S015, and 76% of dark subtracted pixels in engineering grade H2RG-S016 were well fitted by Equation 2. Our criterion for "well fitted" is integrated chi-square probability greater than 0.1. Of the pixels that were not well fitted, those that we examined would have been considered inoperable because they failed one or more operability criteria. Frequently they were obviously noisy, with RTN being one category of noise. Although the large data sets needed for this kind of analysis are not available for science grade SCAs H2RG-006-5.0μm and H2RG-015-5.0μm, nothing was noted in earlier studies suggesting that dark subtracted pixels meeting all operability are nevertheless poorly fitted by the two-parameter model.

read in 2048×2048 pixels at any one time. The expressions for the fitted slope, b, and y-intercept, a, are as follows (Press et al. 1992).

$$b = \frac{n \sum_{i=1}^{n} t_i s_i - \sum_{i=1}^{n} t_i \sum_{i=1}^{n} s_i}{n \sum_{i=1}^{n} t_i^2 - \left(\sum_{i=1}^{n} t_i\right)^2} \tag{3}$$

$$a = \frac{\sum_{i=1}^{n} t_i^2 \sum_{i=1}^{n} s_i - \sum_{i=1}^{n} t_i \sum_{i=1}^{n} t_i s_i}{n \sum_{i=1}^{n} t_i^2 - \left(\sum_{i=1}^{n} t_i\right)^2} \tag{4}$$

In Equations 3-4, we have dropped the (x,y) subscripts for the sake of brevity. The terms a and b must be computed for each pixel.

3.3. Derivation of Equation 1

To correctly model the noise reduction when using multiple non-destructive reads, one must include correlated noise in the integrating charge. Garnett & Forrest (1993) and Vacca, Cushing, & Rayner (2004) have done this using slightly different approaches for sampling-up-the-ramp and MCDS readout modes. However, the JWST readout mode is more general than either of these. Here we extend the previous analysis to cover the more general JWST MULTIACCUM readout mode.

In MULTIACCUM readout, the data are processed in two steps, and both are important for correctly calculating noise correlations. First, the data are averaged into groups of m frames in the on-board FPAP. Subsequently, the n 16-bit unsigned integer averaged groups are downlinked to the ground for line fitting using standard 2-parameter least-squares fitting using Equation 3.

The remainder of this section is necessarily rather mathematical. Readers who are only interested in using Equation 1 to model the noise of a detector system may wish to skip to Section 3.4. Here we introduce no new material, other than that needed to arrive at Equation 1.

Following Garnett & Forrest (1993) and Vacca, Cushing, & Rayner (2004), the variance in the integrated signal from continuously sampled-up-the-ramp data can be calculated using propagation of errors as follows,

$$\sigma_{\text{total}}^2 = (n-1)^2 \sum_{i=1}^{n} \sum_{j=1}^{n} \frac{\partial b}{\partial s_i} \frac{\partial b}{\partial s_j} C_{i,j}, \tag{5}$$

where $C_{i,j}$ is the covariance of the jth data point with respect to the ith data point, and each s_i is the average of m frames. In using Equation 5, we have implicitly assumed that each of the partial derivatives is approximately constant within the range of variation of each s_i (Bevington 1969). If this were not true, we would have to include higher-order partial derivatives. We therefore validate Equation 1 for the baseline NIRSpec readout mode in Section 3.4.

The covariance terms, $C_{i,j}$, are important because the integrating signal randomly walks away from the best fitting line as each successive non-destructive read is acquired. Intuitively, when frame s_i is digitized, the shot noise from frame s_j is already present on the integrating node, and we see that $C_{i,j} = s_j$ for $j < i$. Vacca, Cushing, & Rayner (2004) offer a simple derivation for this relation as follows. For any two reads, i and j, with $j < i$, the associated readout values are s_i and s_j, which are related by

$$s_i = s_j + \Delta_{i-j}, \tag{6}$$

where Δ_{i-j} is the difference in e^- between the two reads. One can now write,

$$
\begin{aligned}
C_{j,i} &= \langle (s_j - \langle s_j \rangle)(s_i - \langle s_i \rangle) \rangle \\
&= \langle s_j^2 \rangle - \langle s_j \rangle^2 + \langle s_j \Delta_{i-j} \rangle - \langle s_j \rangle \langle \Delta_{i-j} \rangle \\
&= C_{j,i} + C_{j,\Delta_{i-j}} \\
&= \sigma_{s_j}^2 \\
&= s_j.
\end{aligned}
$$

Because integrating electrons obey Poisson statistics, we see that $C_{i,j} = s_j$ for $j < i$.

Using Equation 3, the partial derivatives in Equation 5 are found to be,

$$\frac{\partial b}{\partial s_i} = \frac{12i - 6(n+1)}{n(n^2 - 1)}.$$ (7)

Because $C_{i,j} = C_{j,i}$, we can rewrite Equation 5 as follows,

$$\sigma_{\text{total}}^2 = (n-1)^2 \left\{ \sum_{i=1}^{n} \left(\frac{\partial b}{\partial s_i} \right)^2 C_{i,i} + 2 \sum_{i=2}^{n} \sum_{j=1}^{i-1} \frac{\partial b}{\partial s_i} \frac{\partial b}{\partial s_j} C_{i,j} \right\}.$$ (8)

Using Equation 7, and noting that $C_{i,i} = \sigma_i^2$ and $C_{i,j} = s_i$ where i is the first of the two samples to be acquired, Equation 8 can be written,

$$\sigma_{\text{total}}^2 = (n-1)^2 \sum_{i=1}^{n} \left(\frac{12i - 6(n+1)}{n(n^2 - 1)} \right)^2 \left((i-1) t_g f - \frac{1}{2}(m-1) t_f f + \sigma_g^2 \right) + $$ (9)

$$2(n-1)^2 \sum_{i=2}^{n} \sum_{j=1}^{i-1} \frac{12i - 6(n+1)}{n(n^2 - 1)} \frac{12j - 6(n+1)}{n(n^2 - 1)} (j-1) t_g f.$$

In Equation 9, the $\frac{1}{2}(m-1) t_f f$ term is both important and not obvious at first glance. It comes about because each averaged point sampling-up-the-ramp is, strictly speaking, averaged in both the x and y-axis directions. The interval over which shot noise is integrated therefore extends from the mid-point of one group to the midpoint of the next. However, σ_g already includes the shot noise from the beginning of the group to its mid point. For this reason, we must actually *subtract* the $\frac{1}{2}(m-1) t_f f$ term in Equation 9 to avoid overcompensating for this noise. Although the amount of noise accounted for by this term is small, it shows up clearly in the Monte Carlo simulations that were used to validate the model.

To complete the derivation, we need an expression for σ_g. For the ith group, the FPAP performs straight 16-bit integer averaging of the m frames.

$$\langle s \rangle_i = \frac{1}{m} \sum_{k=1}^{m} s_{k,i}$$ (10)

For simplicity, we do not attempt to model truncation errors associated with integer arithmetic. As before, we use propagation of uncertainty to write an expression for σ_g,

$$\sigma_g^2 = \sum_{k=1}^{m} \sum_{l=1}^{m} \frac{\partial \langle s \rangle}{\partial s_k} \frac{\partial \langle s \rangle}{\partial s_l} C_{k,l}. \tag{11}$$

Because the signal within each averaged group is referenced to the first read in that group, the reads on one group are not correlated with those in any other. As such, all groups have the same value of σ_g. Moreover, in this case, the partial derivatives in Equation 11 are both equal to $1/m$, and using Equation 10, we can write the following.

$$\sigma_g^2 = \frac{\sigma_{\text{read}}^2}{m} + \sum_{k=1}^{m} \frac{1}{m^2} (k-1) t_f f + 2 \sum_{k=2}^{m} \sum_{l=1}^{k-1} \frac{1}{m^2} (l-1) t_f f \tag{12}$$

Substituting Equation 12 into Equation 9 and simplifying, we arrive at Equation 1.

3.4. Validation of Equation 1

We have validated Equation 1 using Monte Carlo simulations, by comparing our results to others in the literature, and by modeling real data (see Section 5.2).

3.4.1. Monte Carlo Simulations

To validate Equation 1, we simulated JWST NIRSpec MULTI-22×4 integrations for a range of fluxes. The simulation parameters were as follows; $t_{\text{int}} = 890.4$ s, $\sigma_{\text{read}} = 14$ e^- rms, and $0.001 \leq f < 64$ e^- s^{-1} pixel^{-1}. Because f includes dark current, the lowest flux simulations indicate the ultimate noise floor of the system, while higher flux pixels indicate what might be seen when observing bright stars.

2048×2048 pixel data cubes were simulated by incrementally adding integrated flux one frame at a time. The integrated flux during any one frame time was distributed according

to the Poisson distribution. Once all flux had been accumulated, normally distributed read noise was added to all pixels in all frames. Following plans for JWST operation, the data were then rebinned into n groups of m averaged frames. Finally, Equation 3 was used to compute pixel slopes, these were converted into integrated signal by multiplying by the integration time, and finally the standard deviation of each 2-dimensional 2048×2048 pixel image was calculated.

The results, see Figure 3, are in excellent agreement with Equation 1, with all deviations within the statistical uncertainty of the Monte Carlo simulation.

3.4.2. Comparison to other Authors

It is helpful to consider a few limiting cases for comparison to previous literature results. For the case $m = 1$, straight sampling-up-the-ramp, both Garnett & Forrest (1993) and Vacca, Cushing, & Rayner (2004) contain results that can be compared to our Equation 1. In particular Vacca, Cushing, & Rayner 's Equation 53 is in complete agreement with our result.

In a similar manner, Garnett & Forrest (1993) computed the total noise in read noise dominated and shot noise dominated regimes for continuous sampling-up-the-ramp. For read noise dominated observations, the noise computed using Equation 1 is,

$$\lim_{f \to 0} \sigma^2_{\text{total}} = \frac{12\,(n-1)}{n\,(n+1)} \sigma^2_{\text{read}}, \text{ where } m = 1. \tag{13}$$

For the shot noise dominated regime Equation 1 becomes,

$$\lim_{\sigma_{\text{read}} \to 0} \sigma^2_{\text{total}} = \frac{6\,(n^2+1)}{5n\,(n+1)}\,(n-1)\,t_g f, \text{ where } m = 1. \tag{14}$$

Equations 13 and 14 should compare to Garnett & Forrest 's Equations 19 and 23 multiplied by T^2_{int}. However, they do not, and the difference lies in differing definitions of

the integration time. In Garnett & Forrest (1993), the integration time, T_{int}, is defined as the entire integration time on the detector node, beginning when the reset switch is opened and ending when the final signal level is sample. For most astronomical instruments, this is not correct, and the integration time should be defined as shown in Figure 2.

Expressing t_{int}, the correct integration time in terms of the integration time in Garnett and Forrest's notation, T_{int}, we find,

$$t_{int} = T_{int} - \delta_t = T_{int} \frac{n-1}{n}, \tag{15}$$

where δ_t is the time between successive pedestal or signal samples. With this correction to Garnett & Forrest 's Equations 19 and 23, our Equations 13-14 are in complete agreement with theirs. For completeness, we note that a similar error exists in Garnett & Forrest 's results for Fowler sampling. A correction of the form,

$$t_{int} = T_{int} - \delta_t = T_{int} \left(1 - \frac{1}{2n} \right), \tag{16}$$

should be made to their results for Fowler sampling.

3.5.   Effect of Neglecting Covariance Terms

If covariance terms in Equation 5 are neglected, Equation 1 simplifies as follows,

$$\tilde{\sigma}^2_{total} = \frac{12(n-1)}{mn(n+1)} \sigma^2_{read} + (n-1)t_g f, \tag{17}$$

where we have introduced the new symbol, $\tilde{\sigma}_{total}$, to unambiguously represent the approximate noise. The first term represents read noise being averaged down, and the second term accounts for shot noise on integrated flux under the *incorrect* assumption that noise in the multiple non-destructive reads is uncorrelated.

In the following, we consider two limiting cases: (1) the read noise dominated regime

and (2) the shot noise dominated regime. In both cases, we compare the total noise per pixel computed using Equation 1 to that computed using the approximate relation, Equation 17.

3.5.1. Read Noise Dominated Regime

We first consider the read noise dominated regime. This applies, for example, when measuring the total noise of an SCA having little or no dark current under ultra-low photon flux conditions. JWST SCA H2RG-015-5.0μm was a good example, having dark current ≤ 0.006 e^- s^{-1} pixel^{-1} when tested at the University of Hawaii and at the Space Telescope Science Institute/Johns Hopkins University (Rauscher et al. 2004; Figer et al. 2004). We adopt as our metric the ratio $\xi = \sigma_{\text{total}}/\tilde{\sigma}_{\text{total}}$. For the read noise dominated case, this simplifies to

$$\xi = \lim_{f \to 0} \frac{\sigma_{\text{total}}}{\tilde{\sigma}_{\text{total}}} = 1, \tag{18}$$

and we see that neglecting the covariance terms does not cause significant errors in this case.

3.5.2. Shot Noise Dominated Regime

In the shot noise dominated regime, the situation is very different. Making the simplifying assumption $m = 1$, we compute ξ for straight sampling-up-the-ramp.

$$\xi = \lim_{\sigma_{\text{read}} \to 0} \frac{\sigma_{\text{total}}}{\tilde{\sigma}_{\text{total}}} = 1.095\sqrt{\frac{n^2 + 1}{n(n+1)}}, \text{with } m = 1. \tag{19}$$

From Equation 19, we see that for large n and in the shot noise dominated regime, Equation 17 under-estimates the total noise by 9.5%. As a cross check, we note that this result is consistent with Garnett & Forrest 's Equation 24. Because of this significant error using Equation 17, it is particularly important to use Equation 1 for modeling

sampled-up-the-ramp data when shot noise is important. For completeness, in the baseline NIRSpec MULTI-22×4 readout mode and in the shot noise dominated regime, $\xi = 1.071$ and we see that Equation 17 under-estimates the noise by 7.1%. Equation 1 should clearly be used in this case.

4. Summary of Available SCAs and Test Facilities

The JWST Project began working with Teledyne[5] on the H2RG SCA for space-astronomy in 1998. Two pathfinder SCAs were produced during the development program. These were the 1024×1024 pixel HAWAII-1R, the first Teledyne SCA to incorporate reference pixels in the imaging area, and the 1024×1024 pixel HAWAII-1RG, which added a programable guide window. Although the guide window will be used to some extent by all JWST NIR instruments, it will be most heavily used by the TFI.

Beginning in late 2002, the first science grade H2RGs began to be produced. For purposes of this article, a science grade SCA is one that has excellent performance, but is nonetheless non-flight grade. Reasons why a part might be science grade, instead of flight grade, include differences in packaging and changes in the fabrication process. Table 3 summarizes the properties of all of the SCAs that we discuss in this article. The two science grade parts had serial numbers H2RG-006-5.0μm and H2RG-015-5.0μm. H2RG-006-5.0μm was a fully substrate-removed part whereas the substrate-on H2RG-015-5.0μm was only thinned. Although these two detectors were tested extensively at Teledyne, the University of Hawaii, and at STScI/JHU, these early tests did not include the extensive sets of darks

---

[5]Teledyne Imaging Sensors was formerly known as Rockwell Scientific. To avoid confusion, we will exclusively use the name Teledyne when referring to the company that is making JWST's NIR SCAs.

that are needed for the statistical analysis presented in Sections 5 and 6.

Beginning in 2006, the NIRSpec DS team at GSFC began to receive engineering grade NIRSpec SCAs. Because the packaging was somewhat different to that used earlier, Teledyne hybridized the lowest graded HgCdTe layers first. These lower grade layers have yielded engineering grade detectors with dark current and total noise exceeding NIRSpec requirements. However, these engineering grade detectors were also the first to be used in a fully flight representative MULTI-22×4 readout mode, and with 50 ramps used for each dark current and total noise test. Where possible, we have cross-checked our conclusions based on the large data sets by comparison to available data from the earlier science grade SCAs. For this reason, although the specific performance parameters of these engineering grade SCAs are not fully flight representative vis-à-vis dark current and total noise, we believe that the general conclusions regarding the reset anomaly and RTN are valid. As new and better SCAs arrive, we plan to continue testing these parameters and others to enable the best possible ranking for flight selection.

4.1. Test Facilities

Throughout this article, we refer freely to data acquired in the following test laboratories:

1. NASA GSFC Detector Characterization Laboratory

2. Teledyne Imaging Sensors Test Facility

3. University of Hawaii Test Facility

4. Operations Detector Laboratory at STScI/JHU

In this section, we briefly describe the equipment used in each of these laboratories. We begin, however, with a short discussion of conversion gain, which is used to convert from instrumental analog to digital converter units (ADUs) to electrons. This important parameter is measured by all NIRSpec test laboratories.

4.1.1. Conversion Gain

In recent years, it has become increasingly clear that inter-pixel capacitance (IPC) can significantly affect the conversion gain of hybrid detector arrays like the H2RG (Moore, Ninkov, & Forrest 2004, 2006; Brown et al. 2006). For this paper, which is based on archival data, the photon transfer method was used to measure conversion gain in all laboratories (Janesick, Klaasen, & Elliott 1987), and no correction for IPC was made. Based on our own preliminary IPC measurements, and Brown et al. (2006)'s results for a $\lambda_{co} = 1.7$ μm SCA, we believe that this results in systematic over-estimation of the conversion gain (in units of e^- ADU^{-1}) by about 10%-20% for the measurements that are reported in this article. In other words, the measurements that we report here probably over-estimate the noise, dark current, and DQE by 10%-20%.

For the NIRSpec, we plan to measure IPC by using the H2RG SCA's individual pixel reset capability to directly program pixels to different voltages than their neighbors. We believe that this will allow us to directly measure the crosstalk, and thereby the IPC. This capability is being implemented now, and we plan to begin phasing it into NIRSpec testing starting in late 2007.

4.1.2. NASA GSFC Detector Characterization Laboratory

The NASA GSFC Detector Characterization Laboratory (DCL) is a facility for the design, integration, test, and characterization of detector systems. Major projects include testing detectors for the NIRSpec DS and the Hubble Space Telescope Wide Field Camera 3. The DCL facility that will be used for testing the integrated NIRSpec DS consists of a Class 100 (ISO Class 5) cleanroom and a nearby test control room. The cleanroom houses the test dewar (containing the FPA and SIDECAR ASICs), the room temperature FPE, laboratory array controllers, dewar temperature controllers, optical sources, dewar control, monitoring, and interface electronics, and other support hardware. The control room houses test control and analysis computers, including a Science Instrument Development Unit (SIDU) and a Science Instrument Integrated Test Set (SITS) that communicate with and command the DS. The SIDU and SITS mimic the functionality of the ICDH to facilitate ground-based testing.

The dewar is a custom designed and built cryocooled system from Janis Research Company, Inc. (Model: Pulse Tube Dewar, Serial Number 8862-B). The cooling is provided by a two-stage Cryomech, Inc. Model PT407 pulse tube cryorefrigerator. The dewar is designed to accommodate a NIRSpec FPA containing two Teledyne H2RG SCAs, two Teledyne SIDECAR ASICs, and two NIRSpec flight-design ASIC-to-SCA cables. The temperatures of the mounting fixtures to which the FPA and ASICs mount are independently controlled by heaters and thermometers. The FPA and ASIC mounting plate temperature control, as well as the dewar housekeeping temperature control and monitoring, is provided by LakeShore Cryotronics, Inc. temperature controllers (one model 331 and two model 340s).

Non-flight-design cables connect the ASICs and the FPA thermal control circuits to hermetic connectors on the dewars vacuum shell. External cables connect the ASICs and

FPA thermal control circuits to the FPE. The FPE communicates to the SIDU or the SITS in the control room via Spacewire cables.

For the initial SCA-level tests that are discussed in this paper and diagnostics, another cable is available inside the dewar to bypass the ASIC and ASIC-to-SCA cable, and connect directly to either SCA to allow operating that SCA with laboratory electronics. The laboratory electronics are Generation III controllers from Astronomical Research Cameras, Inc. Within the NIR detector testing community, these are colloquially referred to as "Gen-III Leach Controllers." For this paper, a video gain of about 40× was used, resulting in a median conversion gain, $g \approx 0.9\ e^-\mathrm{ADU}^{-1}$. For SCAs H2RG-S015 and H2RG-S016, the photon transfer method was used to measure the conversion gain of each part. For these parts, the measured median conversion gains were $g = 0.89$ and $0.93\ e^-\ \mathrm{ADU}^{-1}$ respectively. For the testing reported here, the DCL clocked SCAs at 100 kHz per pixel, and the video bandwidth was limited to about 160 kHz using RC filters on the inputs.

4.1.3. Teledyne Imaging Sensors Test Facility

Teledyne Imaging Sensors has developed an infrared detector testing facility to support production testing and flight detector selection for the JWST program. This focus puts emphasis on test throughput, repeatability, and flight documentation. The importance of test throughput is easy to see by looking at the JWST test requirements. The three instruments using HgCdTe detectors on JWST will be producing approximately 180 SCAs for testing. Of these, approximately 20 will be selected as flight-quality. The time period for testing and flight-device selection is only about 1 year. Repeatability of measurements requires a rigorous program of calibration and verification, and includes cross-checking with external laboratories using both reference diode and SCA standards.To eliminate the possibility of operator variability, a highly automated system of acquisition, analysis,

and reporting has been implemented. Lastly, since the SCAs are to be selected for space flight use, significant effort is spent on configuration management, environmental controls, contamination monitoring and control, and documentation.

Three cryostats perform all the testing for JWST. Each of these cryostats can accommodate up to four H2RG sensors in one cooldown. In practice, one of the SCA positions is frequently allocated to a "control" SCA or reference diode to verify test consistency. All of these cryostats are custom designs, and operated with custom electronics and software. Their internal design is such that light-tight labyrinths are included at all mechanical interfaces, consistent with the need for low-background performance at $\lambda = 5 \mu m$ ($f < 0.01\ e^-\ s^{-1}\ pixel^{-1}$). Cooling is provided by CTI mechanical cryocoolers, with the compressors located in the mezzanine above the laboratory. Each cryostat has three separately controlled temperature zones that are cooled from a two-stage cold head. These zones provide for a ~ 30 K inner radiation shield, the 77 K outer radiation shield, and the SCA temperature (typically 37 K).

For low noise testing, the custom readout electronics are operated at a 100 kHz per pixel readout rate and the video bandwidth is limited to about 160 kHz. The video gain of $40 \times$ and 5 Volt analog-to-digital converters combine to yield a typical conversion gain of $\sim 0.477\ e^-\ ADU^{-1}$.

The cryostats have two basic configurations. The "Duomo" configuration has the SCAs viewing a short, squat diffuse-gold dome that is illuminated by internal LEDs. For each wavelength, there are 4 LEDs illuminating the dome at 90° azimuthal spacing. There is enough room around the dome to place LEDs for 7 distinct wavelengths. Because the entire SCA and dome configuration can be cooled to the 37 K operating temperature, this configuration provides the ultimate in dark current capability. Because the LEDs are illuminating the SCAs almost directly, there is very little attenuation of the flux. Two of the

three cryostats are typically used in this configuration, which is capable of demonstrating all flight requirements except for the most stringent DQE measurements. These are limited by the illumination uniformity at the SCAs from this physically compact arrangement (approximately 10 to 15% variability from center to corner) and also the calibration uncertainty of the pulsed measurement (typically ~ 5%).

The second configuration is "Il Campanile." This uses the same configuration of the cryostat as Il Duomo for housing and cooling the SCAs, except that the illumination now comes from a small aperture ~500 mm away from the SCAs. The aperture is fed by an integrating sphere, which in turn is fed by LEDs. The size of the aperture is adjusted to provide the desired intensity of illumination. There are again 7 distinct LEDs that can be commanded to illuminate the integrating sphere. Carefully designed baffles and light traps eliminate stray light. The Il Campanile configuration requires a second, single-stage, cold head for cooling the illumination components to ~77 K.

In normal usage, Il Duomo configurations are used to screen incoming detectors for key performance parameters. The acceptance thresholds (especially for DQE) are set generously in order to avoid discarding potentially acceptable devices. The exact level depends on program requirements, taking into consideration the typical measurement accuracy of the system. After this initial screening, devices that are potentially flight-grade go through a two week period of characterization, at the end of which all performance parameters are reported. For programs requiring DQE measurements better than the ~ 15% level, the best devices are placed in Il Campanile for DQE characterization that can take up to one week. Typical accuracies are wavelength-dependent, but are on the order of 5 to 10%.

For short-wave ($\lambda_{co} = 2.5\ \mu$m) devices, both configurations are sufficiently dark to confirm performance to JWST levels. However, because the Il Campanile has a large physical extent, cooling the baffles and supporting structure to less than ~70 K is impractical.

Consequently, for the mid-wave ($\lambda_{co} = 5\ \mu$m) devices, the Il Campanile configuration will be too warm to reach flight performance levels, but is more than adequate for DQE measurements.

While the main application for these cryostats is JWST testing, they have been successfully used to support other astronomy (low-background) programs, as well as for internal process-development testing. The cryostat design is sufficiently modular to support the differences in mechanical mounting, heat straps, connector pinouts, etc., that could be required for testing many kinds of devices. This flexibility also drives the need for strict configuration management during production testing, as well as a certification program for the test stations after configuration changes.

4.1.4. University of Hawaii Test Facility

The University of Hawaii laboratory was the first test facility to convincingly demonstrate the ultra-low dark current and noise properties of Teledyne $\lambda_{co} = 5\ \mu$m HgCdTe for JWST. These early tests were done using a cryocooled dewar, LakeShore temperature controllers, and a modified Leach controller. Although the University of Hawaii is now testing using SIDECAR ASICs in lieu of Leach controllers, this paper is based on archival data that were taken before the SIDECAR became available. When testing with the Leach controller, the University of Hawaii typically reads out SCAs at a 100 kHz per pixel rate. The video bandwidth is limited to about 160 kHz, and when operated at 40× video gain, the conversion gain is about 1 e^- ADU^{-1}.

For more information about the University of Hawaii test facility, the interested reader is referred to the following publications (Hall et al. 2000, 2004; Hall 2006).

4.1.5.   Operations Detector Laboratory at STScI/JHU

The Operations Detector Lab (ODL) is a joint Space Telescope Science Institute/Johns Hopkins University facility. The primary goal of the ODL is to be able to test flight-like JWST and HST detectors to determine the best way to operate the detectors in flight. This is a different focus that the other JWST labs in that the lab does not try to verify requirements, but instead has the goal to optimize the total science output from the instruments.

Currently, the lab has one IR Labs dewar that uses a CTI model 1050 cryo-cooler to cool both the SCA and internal optics to their operational temperatures (nominally 37 and 60 K respectively). A LakeShore model 340 temperature controller is used to stabilize the temperature of the SCA to within <1 mK per 1000 seconds. A variety of optical configurations are available to either allow direct imaging with a Offner relay, a pinhole camera, or a cryogenic integrating sphere. The detector is housed in a light-tight enclosure where the upper limit on the light leak is 1 photon per 1000 seconds.

The readout electronics use a Generation II controller from Astronomical Research Cameras Inc. Pixels are read out at a 100 kHz per output rate, and the video bandwidth is limited to about 160 kHz using RC filters. The baseline video gain is 40× and the measured conversion gain, $g \approx 1 \ e^- \ \mathrm{ADU}^{-1}$.

For more information on the ODL's test setup, the interested reader is referred to Figer et al. (2003).

5.   Reset Anomaly

It is not uncommon to observe a reset anomaly in MULTIACCUM sampled data from JWST H2RGs (Figure 4). The anomaly is characterized by non-linearity in the early frames

following pixel reset. Although the reset anomaly appears to be unrelated to response linearity[6], these early frames nonetheless fall below below a line projected through the later, asymptotic portion of the ramp. Fortunately, the reset anomaly is nearly noiseless for JWST SCAs that have been tested so far, and it usually subtracts out during dark or sky subtraction. Nevertheless, its potentially detrimental side effects must be considered for the most accurate measurement of dark current.

Depending on the part, we have found that the fraction of affected pixels can range from just a few percent to a significant fraction of the SCA. Tests of the engineering grade $\lambda_{co} = 5$ μm NIRSpec SCA H2RG-S016 revealed that over 15% of pixels could not be satisfactorily modeled by a straight line ($Q_{line} < 0.1$). Here, Q is the integrated chi-square probability density giving the probability that the fit's χ^2 could have been obtained by chance fluctuation within the error bars (Press et al. 1992, Equation 6.2.3). On the other hand, the reset anomaly was barely noticeable in at least one outstanding prototype SCA, H2RG-015-5.0μm. This detector is one of four JWST SCAs in regular use at the University of Hawaii 2.2-m telescope (Hall et al. 2004).

The reset anomaly can introduce systematic errors into dark current measurements if it is not correctly accounted for. As illustrated in Figure 4, if a 2-parameter line is fitted through all points, the early frames cause the fitted line to over-estimate the asymptotic slope, and thereby the dark current.

One common solution is to discard the first few frames of each integration. Clearly, this is an inefficient use of time. Furthermore, complete and unbiased removal of the reset anomaly is non-trivial. For JWST SCAs, the reset anomaly has been observed to have time constants ranging from seconds to hours before the pixels reach the asymptotic portion of

---

[6]For NIRSpec, we plan to confirm this by test of the integrated DS.

the ramp. Moreover, different pixels in the same SCA have different time constants. Even by discarding the first few frames, it is difficult to consistently identify the asymptotic portion of the ramp, and a systematic bias tending to over-estimate the dark current remains.

A solution that does not require discarding data is to extract the asymptotic slope using a function that allows for the reset anomaly early in the ramp. Recent JWST testing has demonstrated that MULTIACCUM sampled data from pixels showing the reset anomaly can be well-modeled by a 4-parameter function that includes linear and exponential components. We speculate that the exponential term may be related to RC charging effects in the ROIC/detector components of the hybrid. The equation is of the form,

$$s_{x,y}(t) = a_{x,y} + b_{x,y}t + c_{x,y}\exp(d_{x,y}t), \tag{20}$$

where $s_{x,y}$ is the integrating signal, t is time, and $a_{x,y}$, $b_{x,y}$, $c_{x,y}$, and $d_{x,y}$ are the four fitting parameters. The parameters $c_{x,y}$ and $d_{x,y}$ are negative quantities. Bacon et al. (2004) used the same equation for modeling the dark current of pixels in a $\lambda_{co} = 9.1$ μm detector array made by Teledyne when they were known as Rockwell Scientific. Of the non-linear pixels ($Q_{line} < 0.1$), more than 70% are well fitted by the 4-parameter model ($Q_{4-param} > 0.1$). Of the remaining non-linear pixels, many were hot pixels or were corrupted by RTN (see Section 6).

Figure 4 shows a direct comparison of all three fitting methods. The data are taken from a single pixel in a dark integration. A linear fit of the entire ramp clearly overestimates the dark current. The linear fit of the asymptotic portion of the ramp and the 4-parameter fit provide much better results. Although both of these methods are comparable in their quality of fit, the 4-parameter fit does not require any data to be discarded. Furthermore, the asymptotic portion of the ramp does not have to be identified for each pixel in the array.

5.1. Noiseless Calibration of the Reset Anomaly

NIRSpec testing has shown that the reset anomaly is highly repeatable for a given pixel. A direct comparison of populations of pixels that both are and are not affected by the reset anomaly indicates that the reset anomaly contributes almost no additional noise (Figure 5). Although the dark current properties of these engineering grade SCAs are unacceptable for NIRSpec, the noise properties of the two populations are essentially identical.

We cross-checked these conclusions against science grade SCA H2RG-006-5.0μm. Although the available data sets do not allow us to make the same statistical comparison that we make above for more recent parts, we have compared the measured total noise using 88 samples taken at the beginning of MULTI-145×1 sampled integrations to 88 samples taken at the very end. In this case, we find that using the first 88 frames degrades the total noise by only a few percent compared to using the last 88 frames. We used 88 frames as the basis of this comparison because the NIRSpec baseline MULTI-22$times$4 readout mode allows 88 frames per 1008 seconds integration.

The reset anomaly calibrates out during matching dark or sky subtraction. Figure 6 shows the subtraction of a median dark integration from an individual dark integration. The subtraction is performed using a matching MULTI-88×1 median dark cube, which was created from a median combination of 50 individual dark integrations, pixel-by-pixel, within the 2048×2048×88 pixel cube. The subtracted images have offsets and residual slopes, which are the equivalent to $a_{x,y}$ and $b_{x,y}$, respectively, in Equation 2. The distribution of offsets is centered at zero, which indicates that the reset anomaly has an identical shape from one integration to the next. The scatter in the offset, $a_{x,y}$, is completely dominated by kTC noise associated with resetting the pixel at the beginning of the integration. In Section 5.2, we show the small residual slope is consistent with shot noise on integrating

dark current as predicted by Equation 1 with $f = i_{\text{dark}}$.

5.2. Unbiased Dark Current Measurements

We tested the success of the 4-parameter model for measuring dark current using real data from NIRSpec H2RGs. In particular, we (1) tested whether the dark current inferred from the 4-parameter fit could account for the observed noise of the test SCAs and (2) compared the success of the 4-parameter fit to the more traditional methods discussed above. These tests included a statistical analysis of the noise properties of pixels in engineering grade NIRSpec SCAs H2RG-S015 and H2RG-S016. We also performed less extensive spot checks on engineering grade NIRSpec SCA H2RG-S002.

We expect the measured total noise to be about equal to the noise predicted by Equation 1. The observed noise per pixel is given by the standard deviation in the pixel's integrated signal over many integrations. We analyzed 50 individual integrations taken in the DCL, as described in Section 4.1.2. To remove the instrumental signature of the reset anomaly, we subtracted a median dark integration from each individual integration. As described in Section 5.1, the reset anomaly is highly repeatable. A nearly noiseless subtraction was obtained, as illustrated in Figure 6. The subtraction for each pixel generally results in a small residual slope, $b_{x,y}$, with an offset, $a_{x,y}$.

To calculate the noise for each pixel (x,y), we fitted a 2-parameter line to the residual slope in each of the 50 dark subtracted integrations using Equation 2. The $a_{x,y}$ term, which is completely dominated by kTC noise, was discarded. The $b_{x,y}$ term was used to calculate the integrated signal as follows,

$$s_{x,y} = b_{x,y} t_{\text{int}}. \tag{21}$$

The analysis produced 50 2-dimensional images of the residual signal. As expected, the

mean value of each pixel is zero e^- to well within the uncertainties. The noise of each pixel was computed as follows,

$$\sigma_{\text{total}}[x,y] = \left(\frac{1}{n-1} \sum_{i=1}^{n} (s_i[x,y] - \langle s[x,y] \rangle)^2 \right)^{1/2} \text{ where n = 50.} \tag{22}$$

Ideally, we expect the measured noise (Equation 22) to equal the modeled total noise (Equation 1). In other words, the ratio of measured to model noise values should be 1.0. In Equation 1, the variable f is the dark current of each pixel measured using the 4-parameter fit. The read noise per frame, σ_{read}, is approximated using the spatial averaging technique. In spatial averaging, two correlated double sampling (CDS) integrations, INT0 and INT1, are used to infer the average noise. Each CDS integration is represented by a data cube. The first two dimensions are the (x,y) pixel position, and the 3rd dimension gives the sample number which can have the value 0 or 1. σ_{read} was calculated as follows,

$$\sigma_{\text{read}}^2 = \frac{1}{2}\text{stdev}\left((\text{INT1}[*,*,1] - \text{INT1}[*,*,0]) - (\text{INT0}[*,*,1] - \text{INT0}[*,*,0])\right). \tag{23}$$

Because statistical outliers can corrupt spatial averaging noise measurements, iterative sigma clipping with a 3σ threshold was used to reject outliers.

We analyzed the noise characteristics of pixels with the reset anomaly in SCAs H2RG-S015 and H2RG-S016. The dark current used in Equation 1 was obtained from the 4-parameter fit. For each pixel, the measured noise was compared to the mean predicted noise. The results are shown in Figure 8. The success of the 4-parameter fit is highlighted by the agreement between the measured and modeled noise values. The ratio of the two noise terms for SCAs H2RG-S015 and H2RG-S016 are 0.97 and 1.02, respectively. These ratios are for the modes of the distributions.

For comparison purposes, the dark current was also measured using the other fitting techniques described above: (1) linearly fitting the entire ramp and (2) linearly fitting the asymptotic portion at the end of the ramp. For consistency, the asymptotic portion of the

ramp was designated to be sample numbers greater than 50. The results in Figure 8 indicate that a linear fit of the entire ramp is a poor estimate of the dark current. The measured and modeled noise values do not agree within an acceptable uncertainty. The linear fit of the asymptotic portion at the end of the ramp does much better. The results are comparable to the 4-parameter fit. The ratio of the two noise terms for SCAs H2RG-S015 and H2RG-S016 are 1.01 and 1.00, respectively. While this method provides adequate results, it requires data to be discarded and does not provide consistent results due to varying time constants.

While we are encouraged by the excellent agreement between measured and modeled noise for these SCAs, this agreement depends in part on the conversion gain, g. As explained in Section 4.1.1, conversion gain was measured using the photon transfer method (Janesick, Klaasen, & Elliott 1987), and for consistency in this argument we used the mode of the distribution of g values for each SCA. Ideally, g would be individually measured for each pixel, and an IPC correction would be applied. Doing this accurately requires larger data sets than are available for these engineering grade parts, and better knowledge of the IPC than is available at the present time. We therefore plan to revisit the agreement between measured and modeled noise as more complete data sets, including good measurements of IPC, become available for NIRSpec's flight and flight spare SCAs in late 2007 and 2008.

5.3. Note on Obtaining Convergence in 4-Parameter Fitting

We used the IDL procedure CURVEFIT for 4-parameter fitting. Unfortunately, we find that it is often necessary to have good first-estimates of the 4-parameters in advance of fitting a pixel to ensure convergence. For the statistical analysis that are reported here, a small set of pixels was studied to determine reasonable starting coefficients for all pixels in the data set. A fully automated approach is clearly preferable, and we plan to explore this further in future publications.

6. Random Telegraph Noise

In this section, we show that large-amplitude RTN affects a small and fixed population of pixels. This confirms a previous finding by C. McMurtry (pers. com. 2004). We believe that small-amplitude RTN, close to the noise floor of the SCA, can probably be tolerated so long as it does not cause pixels to exceed their stringent total noise budgets. If substantiated by future testing of NIRSpec flight SCAs, we plan to monitor and track RTN using standard pixel operability maps.

RTN has been observed in several JWST H2RG SCA's, as well as in four H1RGs at the University of Rochester (Bacon et al. 2005). RTN is characterized by a digital-like toggle between two (or more) levels. For this reason, RTN has also been referred to as "popcorn mesa noise" (Rauscher et al. 2004) and "burst noise" (Bacon et al. 2005). Because RTN has been observed in both regular and reference pixels, the noise is thought to originate in the ROIC. One likely explanation points to single-charge defects in the unit cell MOSFET, which is the first amplifier seen by a detector diode.

Figure 8 illustrates a few manifestations of RTN in JWST H2RG pixels. In each case, the data are distributed between two (or more) distinct states. The distribution characteristics of these states, however, vary from pixel to pixel. In particular, the states can vary in size, and the frequency and magnitude of the scatter.

These variations make the detection of RTN difficult and time consuming. We have developed a simple algorithm to detect RTN pixels in MULTIACCUM sampled data. The algorithm consists of a two step process designed to identify pixels that share the following two characteristics: (1) unusually noisy sample ramps and (2) sharp rises and falls associated with the digital toggle between the two states.

The first step identifies noisy ramps. Consider a typical pixel with RTN (e.g.

Figure 9(a)). To remove any offsets and correlated noise effects, a median dark integration is subtracted from the individual integration (Figure 9(b)). The noise in this ramp is revealed by the large degree of scatter. Two distinct readout states are revealed. While these two states are apparent in Figure 9(b) by inspection, they are more clearly illustrated by the histogram in Figure 9(c). The scatter in these pixels tends to be larger than the average scatter, σ_{avg}. We flag all pixel ramps with a sample scatter beyond $\pm 5\sigma_{\mathrm{avg}}$ as potential RTN pixels. Although this high threshold has the advantage that it results in few false detections, it also means that we miss smaller amplitude RTN pixels.

This first step, however, cannot distinguish between RTN pixels and pixels that are naturally noisy. The algorithm tends to return false detections due to "hot" pixels that do not necessarily exhibit the two (or more) distinct states that are associated with RTN. These pixels have a high degree of scatter because they typically have high dark current and poor median dark subtraction. For future detector operation, we expect to have pixel masks which will allow us to identify and avoid these "hot" pixels. At the time of this analysis, however, we implemented a second step to isolate RTN pixels.

This second step identifies pixel ramps that exhibit sharp, distinct rises and falls. This characteristic is typical of RTN, which is identified by the toggling between two (or more) levels. In comparison, the noise in "hot" pixels is due to large dark current and does not tend to toggle up and down. Instead, the charge increases steadily, just as it does in well-behaved pixels. The only difference is that the increase tends to be larger. Differencing successive data points provides an easy analysis of the pixel behavior. The toggle in an RTN pixel will produce a differential plot similar to the one shown in Figure 9(d). Again, the pixel differentials will have an average scatter, σ_{avg}. Of these pixels flagged in step one, all ramp differentials with scatter beyond $\pm 5\sigma_{\mathrm{avg}}$ are flagged as RTN pixels.

The success of this algorithm is highlighted by its false detection rate of less than

1%. Nonetheless, we note that the algorithm's success is limited by the chosen threshold. For the present purpose of studying RTN characteristics, we choose a $\pm 5\sigma_{avg}$ threshold to best isolate pixels with RTN from pixels that may be affected by other noise sources. Therefore, our sample of RTN pixels represents a lower limit on the actual number of RTN pixels within the array. A ramp could potentially have two states confined within the $5\sigma_{avg}$ threshold and would thereby go undetected. Setting the threshold lower would increase the number of detections but it would also increase the chance of a false detection due to the other sources of scatter. A possible solution utilizes multiple-Gaussian fitting to identify the two unique populations apparent in Figure 9(c) (Bacon et al. 2005).

Using our 2-pass algorithm, we have observed large-amplitude RTN to occur in a fixed, small subset of pixels. For SCA H2RG-S16, 99 integrations were tested. Figure 10 shows a histogram which illustrates the repeatability of RTN detections per pixel from integration to integration. A vast majority of pixels have zero detectable RTN features at the $\pm 5\sigma_{avg}$ threshold in any of the 99 integrations sampled, as indicated by the peak at bin 0, which reaches beyond the extent of the plot to just under 100%. Less than 1% of pixels exhibited RTN characteristics at the $\pm 5\sigma_{avg}$ threshold. For a majority of those that did, RTN was subsequently detected in that pixel for 99% of integrations, as indicated by the peak at bin 99. The noticeable rise in bin 1 and fall off in bin 100 is a result of the statistical nature of the magnitude of the scatter. These features can also be partly attributed to the algorithm's $< 1\%$ false detection rate.

For the engineering-grade JWST SCAs that have been studied to-date, these results for H2RG-S16 are typical, and only a small percentage of pixels appear to show large-amplitude RTN at T=37 K. Using a more sensitive detection algorithm, Bacon et al. (2005) found that 11% of the pixels in the SCA that they tested manifested RTN at T=37 K, and moreover that there were significant temperature dependencies. These included the size of

the largest transition decreasing with increasing temperature (Bacon et al. 2005). The difference in the percentage of RTN pixels reflects differences in detection algorithms, and possibly device-to-device variation.

As science and flight grade SCAs become available for JWST, we plan to continue and extend these studies of RTN. One interesting conjecture is that there may be a continuum of pixels affected by RTN (blending into the read noise), and that the lower one sets the threshold, the more RTN pixels one finds. Even if this conjecture were substantiated, however, it is not clear to us that a pixel should be disqualified from use if it meets all operability requirements while manifesting low-level RTN. At some level, RTN becomes one of many components that contribute to the overall noise of a pixel. Viewed in this light, RTN is a noise component that has the advantage that it is easily identified, and therefore fixed in future SCA designs.

The repeatability of large-amplitude RTN is good news. The feature is typically one of the noise components that can cause a pixel to fail to meet operability requirements. Locating and handling RTN pixels in real time pipelined processing is costly and inefficient. Because large-amplitude RTN is confined to a fixed, small subset of pixels, it is a feature that can be tracked using a pixel operability mask. Because tracking operable pixels is a standard part of calibration for flight instruments, we expect large-amplitude RTN to have a negligible impact on JWST calibration pipelines.

7. Suggestions & Plans for Future Work

Additional study is needed to understand how repeatable small-amplitude RTN is. Although we hypothesize that small-amplitude RTN is also a property of a fixed population of pixels, it would be good to confirm this by test. Doing this correctly requires a better

RTN detection algorithm than we have at the current time, and we plan to test this hypothesis as better detection algorithms are developed.

Likewise, it would be helpful to know exactly where in the signal chain RTN arises. We know that a significant fraction of the RTN, perhaps all of it, originates in the ROIC. We know this because we see RTN in both reference pixels, which are not connected to the HgCdTe detectors, and regular pixels. Others have also used specialized readout software to show that RTN originates in the ROIC (Bacon et al. 2004). Simple physical arguments suggest that the origin lies in the first MOSFET in the signal chain, although it would clearly be better to experimentally pinpoint the origin. Doing this could facilitate design improvements to eliminate the RTN.

For similar reasons, it would be helpful to identify the physical mechanism that is the underlying cause of the reset anomaly. As with RTN, additional study would be helpful. One area that we plan to explore more fully is whether the reset anomaly alters a pixel's response to light. Although there has been no clear evidence of this in the JWST program so far, it will be tested when we characterize the linearity and photometric stability of the DS.

8. Summary

In this paper, we describe the JWST NIRSpec's baseline MULTIACCUM readout mode, present a general noise model for NIR detector data acquired using multiple non-destructive reads, and discuss recent NIRSpec SCA test results. We believe that the noise model is applicable to most astronomical NIR instruments. Our major findings and recommendations are as follows.

1. The total noise in common NIR detector operating modes, including CDS, MCDS (Fowler-N), and MULTIACCUM, can be modeled using Equation 1 and the parameters listed in Table 2. This noise model includes read noise, shot noise on integrated charges, and covariance terms between multiple non-destructive reads. If these covariance terms are neglected, and read noise and shot noise are simply added in quadrature, we show that errors of $\approx 9.5\%$ in the predicted noise for bright sources are possible. The sense of the error is to under-predict noise when covariance terms are neglected.

2. Many NIRSpec H2RG SCAs have shown a reset anomaly. This appears as non-linearity in the early reads following reset. Although the reset anomaly does not appear to be related to response linearity, we plan to verify this by test for NIRSpec. If the reset anomaly is not correctly accounted for during calibration, it can lead to systematic over-estimation of the dark current. We show how the reset anomaly can be noise-lessly calibrated out using matching darks, and how dark current can be accurately measured in the presence of the reset anomaly using 4-parameter fits.

3. As has previously been reported, NIRSpec H2RGs are often affected by RTN. Using new test data, we show that large-amplitude RTN is often a property of only a small and fixed population of pixels. For flight operations, we plan to monitor and track RTN using pixel operability maps.

These conclusions, particularly with regard to the reset anomaly and RTN, are largely based on testing engineering grade SCAs. This was done because the required large data sets are only available from engineering grade parts at this time. We therefore plan to confirm these findings using better SCAs as they become available.

REFERENCES

Arendt, R.G., Fixsen, D.J., & Moseley, S.H. 2002, ASP Conf. Ser., 281, 217

Bevington, P.R. 1969, "Data Reduction and Analysis for the Physical Sciences", McGraw Hill:New York

Bacon, C.M., McMurtry, C.W., Pipher, J.L., Forrest, W.J., Garnett, J.D., Lee, D., & Edwall, D.D. 2004, Proc. SPIE, 5563, 35

Bacon, C.M., McMurtry, C.W., Pipher, J.L., Forrest, W.J., & Garnett, J.D. 2005, Proc. SPIE, 5902, 116

Brice, J.C. 1987, "Properties of Mercury Cadmium Telluride", Eds. J. Brice & P. Capper, INSPEC, Institution of Electrical Engineers: London & New York

Brown, M., Schubnell, M., & Tarle, M. 2006, PASP, 118, 000

Figer, D.F. et al. 2003, Proc. SPIE, 4850, 981

Figer, D.F., Rauscher, B.J., Regan, M.W., Morse, E., Balleza, J., Bergeron, L., & Stockman, H.S. 2004, Proc. SPIE, 5167, 270

Fowler, A. & Gatley, I. 1991, Proc. SPIE, 1541, 127

Gardner, J.P. 2006, Space Science Reviews, Vol. 123, No. 4

Garnett, J.D. & Forrest, W.J. 1993, Proc. SPIE, 1946, 395

Hall, D.N.B., Hodapp, K.W., Goldsmith, D. L., Cabelli, C., Haas, A. K., Kozlowski, L. J., & Vural, K. 2000, Proc. SPIE, 4008, 1268

Hall, D.N.B., Luppino, G., Hodapp, K.W., Garnett, J.D., Loose, M., & Zandian, M. 2004, Proc. SPIE, 5499, 1

Hall, D.N.B. 2006, "Development of Advanced Near Infrared Focal Plane Technology for Origins/Next Generation Space Telescope: Final Technical Report", Report submitted to NASA Ames Research Center for contract NAS 2-98077

Janesick, J.R., Klaasen, K.P., Elliott, T. 1987, Optical Engineering, 26(10), 972

Moore, A.C., Ninkov, Z., & Forrest, W.J. 2004, Proc. SPIE, 5167, 204

Moore, A.C., Ninkov, Z., & Forrest, W.J. 2006, Optical Engineering, 45(7), 076402-1

Press, W.T., Teukolsky, S.A., Vetterling, W.T., & Flanney, B.P. 1992, "Numerical Recipes in C, the Art of Scientific Computing; 2nd ed.", Cambridge University Press

Rauscher, B.J. et al. 2004, Proc. SPIE, 5487, 710

Rauscher, B.J. & Hill, R.J. 2007, "James Webb Space Telescope Near-Infrared Detectors TRL-6 Demonstration", NASA Report submitted to the JWST Technology Non-Advocate Review Panel

Vacca, W.D., Cushing, M.C., & Rayner, J.T. 2004, PASP, 116, 352

Table 1.   Driving NIRSpec Detector Performance Requirements

Parameter	Requirement	Comment
Total noise (e^- rms)	6	$t_\text{int} = 1008$ s
		multi-22×4
Mean dark current ($e^-\text{s}^{-1}\text{pixel}^{-1}$)	0.010	
DQE	70%	$0.6 \leq \lambda < 1.0\mu$m
	80%	$1 \leq \lambda < 5\mu$m
Operating temperature (K)	34-37	
Pixel operability for science[1]	>92%	

[1]Pixel operability for science includes stringent thresholds on total noise and DQE. Pixels that fail to meet the operability for science requirement are degraded, although they may still be useful for target acquisition and other less sensitive observations.

Table 2.   Model Parameters for Common Readout Modes[1]

Readout Mode	n	m	Comments
MULTI-22×4	22	4	JWST NIRSpec baseline
MULTI-6×8	6	8	JWST NIRCam baseline
CDS	2	1	Correlated double sampling
MCDS-8[2]	2	8	Also known as Fowler-8
MCDS-16	2	16	Fowler-16
MCDS-32	2	32	Fowler-32

[1]For many astronomical detector arrays, the read noise per frame is approximately $\sigma_{\mathrm{read}} \approx \sigma_{\mathrm{CDS}}/\sqrt{2}$. This approximation is appropriate for short dark integrations, for which shot noise on integrated dark current is negligible compared to read noise.

[2]For MCDS readout modes, $t_g = t_{\mathrm{int}}$.

Table 3. Summary of JWST NIR SCAs[a]

Serial Number	Grade	σ_{CDS} (e^- rms)	σ_{total} (e^- rms)	i_{dark} (e^- s^{-1} pixel^{-1})	QE 1.25 μm	QE 2.2 μm	Crosstalk	Persistence
H2RG-006-5.0μm	sci	12.5[c]	6[b,c]	.004[c]	...	...	...	...
H2RG-015-5.0μm	sci	...	5.88[d]	.006[c]	95%[c]	95%[c]	1.56%[d]	0.1%[d]
H2RG-S015	eng	12.3[e]	16.5[e]	0.28[e]	...	...	...	
H2RG-S016	eng	14.5[e]	8.6[e]	0.004[e]	...	...	...	

[a]All tests were performed at T=37 K. The detectors were biased to meet the NIRSpec well-depth requirement of 6×10^4 e^-.

[b]MCDS-16 sampling (Fowler-16) was used for this early measurement. For all other σ_{total} measurements, which were made later, NIRSpec-baseline MULTI-22×4 sampling was used.

[c]Rauscher & Hill (2007)

[d]Figer et al. (2004)

[e]NASA GSFC Detector Characterization Laboratory measurement.
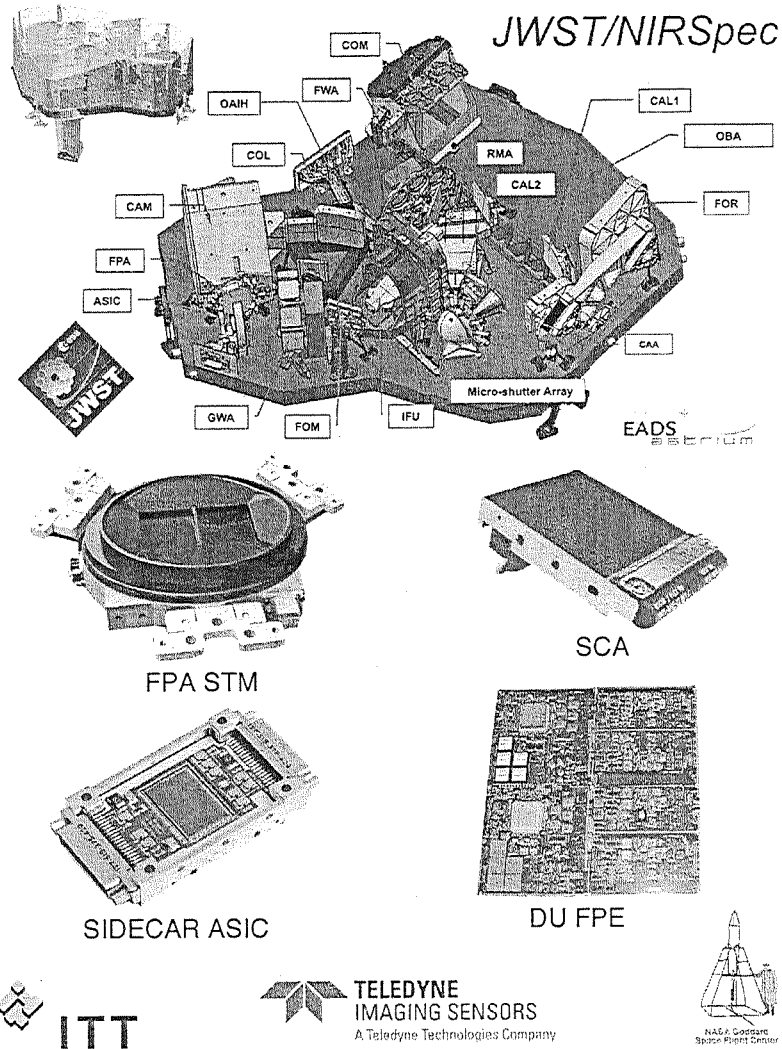
Fig. 1.— NIRSpec is being built by EADS/Astrium for the European Space Agency. NASA is providing the detector subsystem (DS), which is the focus of this paper, and the micro-shutter array for target selection. DS components include the focal plane assembly (FPA). Here we show the structure and thermal model (STM) during test at ITT. The FPA contains two Teledyne HAWAII-2RG sensor chip assemblies (SCAs). Other components include two SIDECAR ASICs for FPA control and the focal plane electronics (FPE), which control the SIDECARs. This figure shows a development unit (DU) of the FPE undergoing test at NASA GSFC.
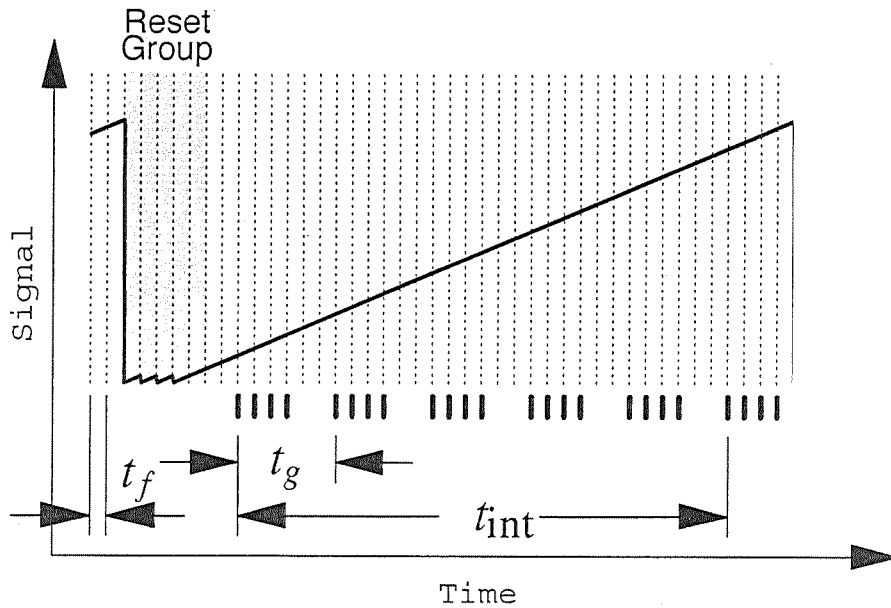
Fig. 2.— JWST's NIR detectors use MULTIACCUM sampling. The detector is read out at a constant cadence of one frame every $t_f \approx 10.5$ seconds. Although frames are clocked and digitized at a constant cadence, to conserve data volume, not all frames are saved. In this figure, saved frames are indicated by short, double width lines. Likewise, to conserve downlink bandwidth, not all frames are downlinked to the ground. Saved frames are co-added in the FPAP and averaged, resulting in one averaged group of data being saved to the solid state recorder every t_g seconds. The resulting FITS file, consisting of a sampled-up-the-ramp data cube with points spaced at t_g intervals, is downlinked to the ground for further processing.
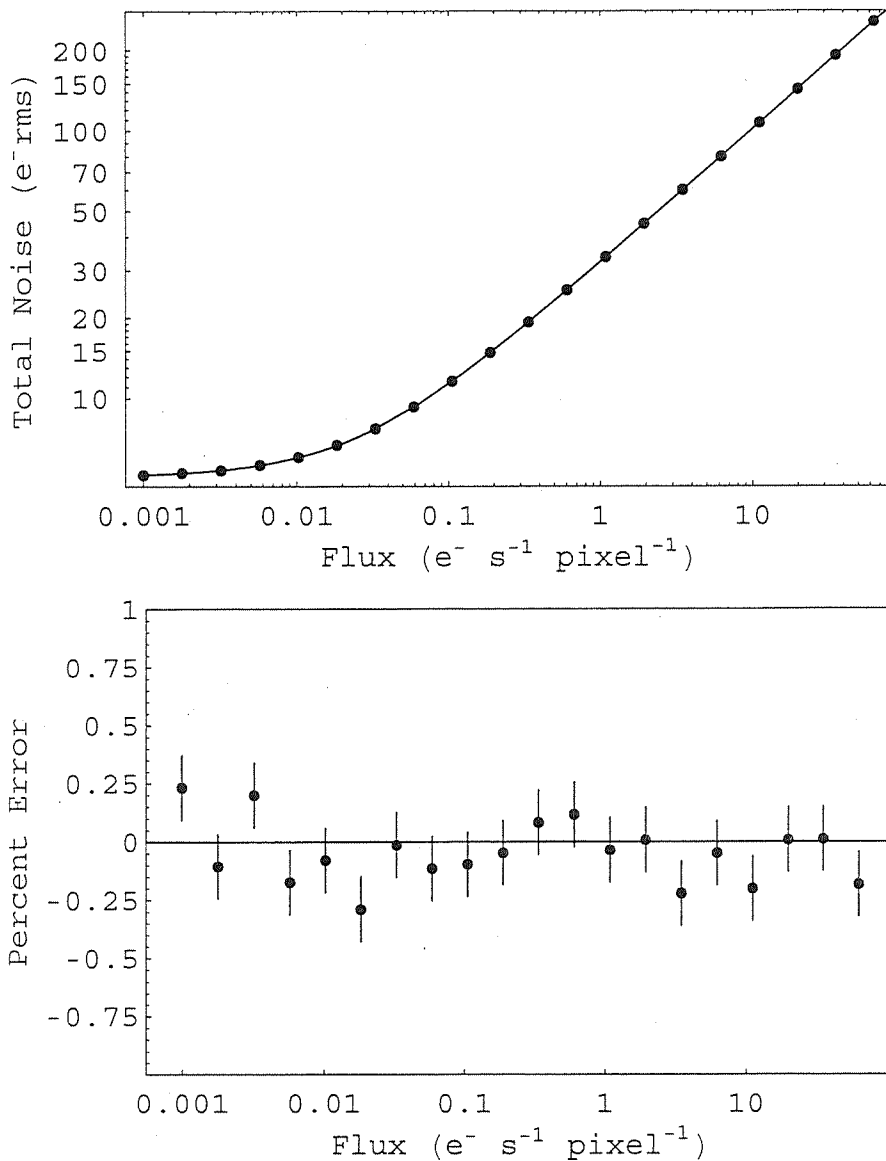
Fig. 3.— Equation 1 was validated using Monte Carlo simulation of NIRSpec's MULTI-22×4 readout mode. The integration time was $t_{int} = 890.4$ s, the read noise was $\sigma_{read} = 14$ e^-, and dark current is included in the flux, f. The top panel shows total noise computed using Equation 1 (solid line) and data points from 20 Monte Carlo simulations using approximately 10^6 pixels per simulation. The bottom pane shows the percent error computed under the assumption that the Monte Carlo points represent truth.
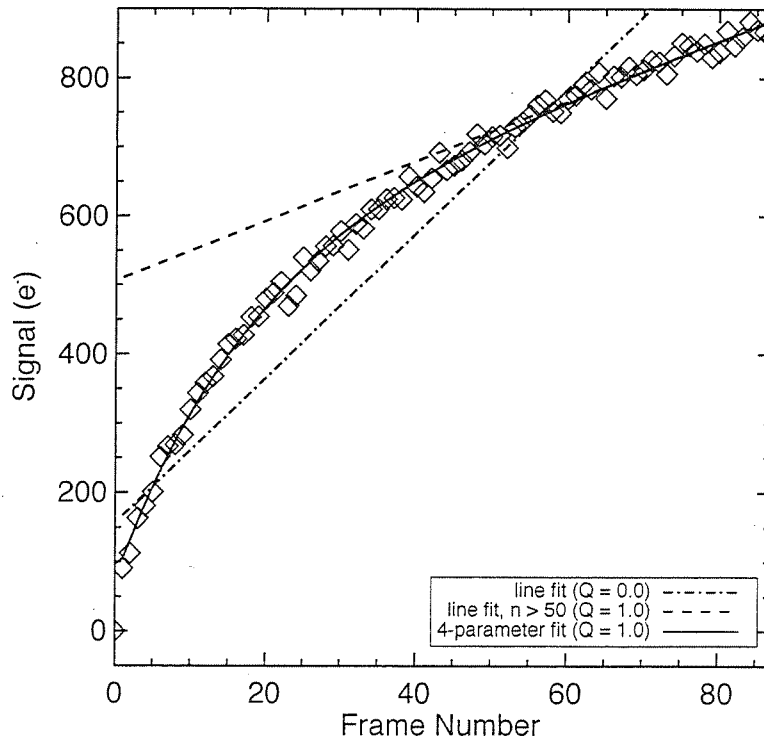
Fig. 4.— The reset anomaly is a common nonlinear effect in the early frames following pixel reset. Here we show the 88 samples-up-the-ramp for a pixel from engineering grade SCA H2RG-S016. The early samples fall below the best fitting line drawn through later samples (dash). If a linear fit is attempted through all the data points, the early frames cause the fitted line (dash-dot) to over-estimate the dark current. The best fit for the entire data set (solid) indicates a four parameter equation that combines both exponential and linear terms. The goodness of fit is given by chi-square probability function, Q.
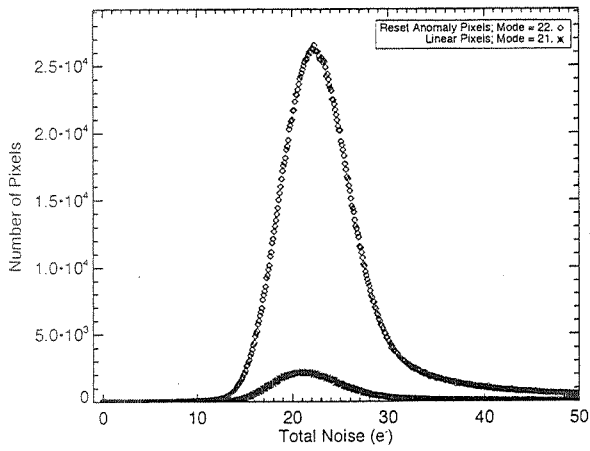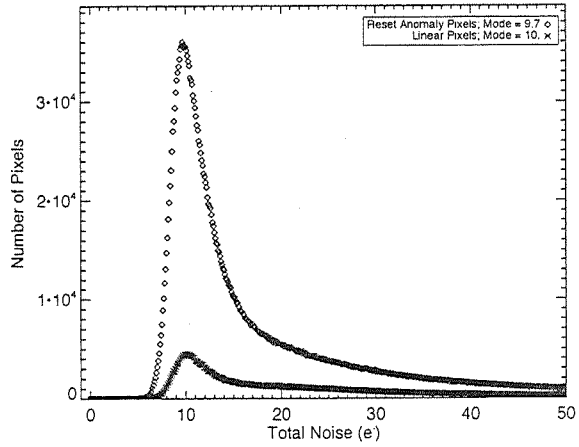
(a) H2RG-S015   (b) H2RG-S016

Fig. 5.— The reset anomaly is nearly noise-less. Here we compare the measured total noise for pixels having a significant reset anomaly to a population of pixels that do not have the reset anomaly drawn from the same SCA. Apart from normalization, the properties of the two distributions do not differ significantly.
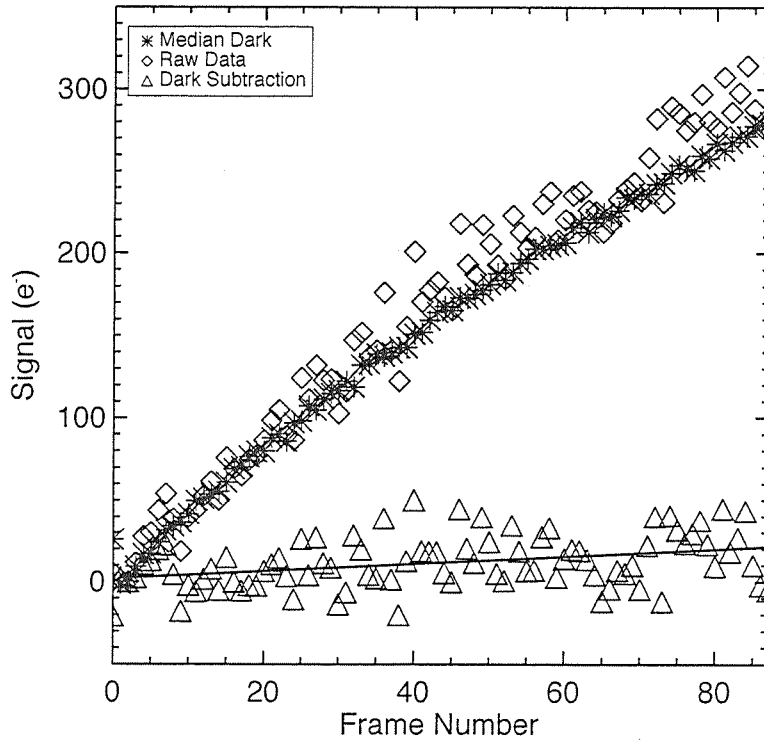
Fig. 6.— The reset anomaly is a nearly noiseless instrument signature that can be removed by subtracting a matching median dark cube (stars) from an individual science integration (diamond). Here we show the 88 samples-up-the-ramp for a pixel from engineering grade SCA H2RG-S016. The data are shown before (diamond) and after (triangle) matching dark subtraction.
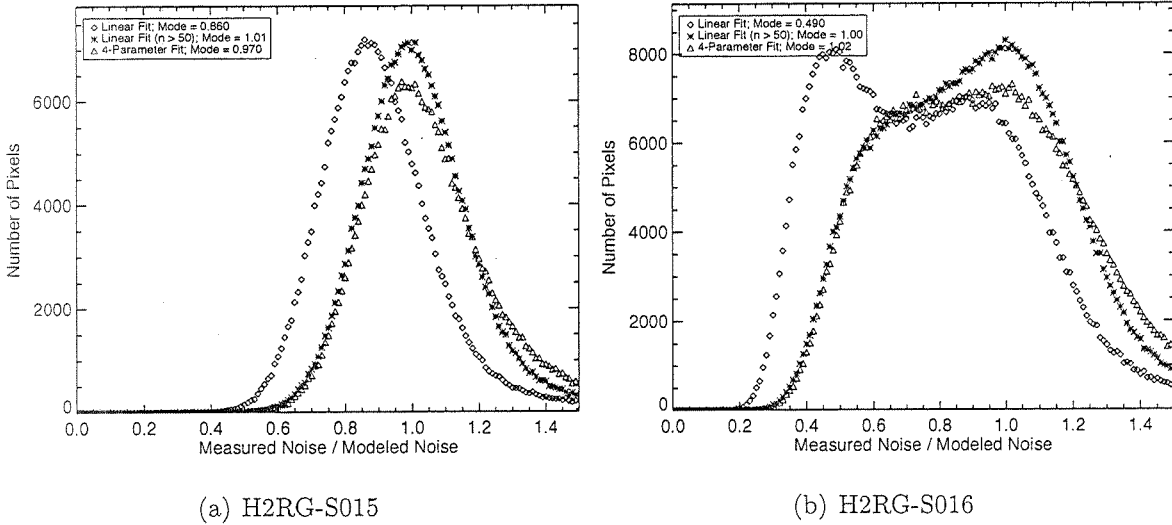
(a) H2RG-S015   (b) H2RG-S016

Fig. 7.— These plots provide histograms of the ratio of the measured noise to modeled noise for pixels in an SCA that can be characterized by the reset anomaly. The x-axis represents a pixel's average ratio taken from 50 individual integrations. The y-axis is the frequency of the given ratio. The measured noise is calculated from Equation 22, where σ_{total} is the standard deviation in a pixel's signal over 50 individual integrations. The modeled noise is derived from Equation 1, where f is the measured dark current in an individual data ramp. The three populations represented are the three different methods of measuring dark current: a linear fit on the entire ramp, a linear fit on the asymptotic portion of the ramp, and the 4-parameter fit. The latter two provide a very good estimate of the dark current, while the linear fit of the entire ramp tends to overestimate the linear slope.
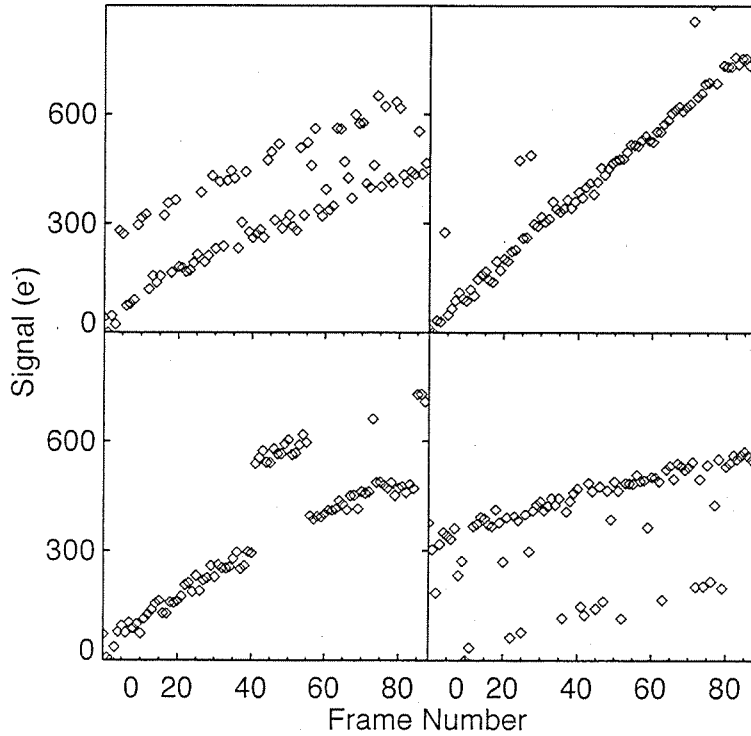
Fig. 8.— Random Telegraph Noise (RTN) is an artifact characterized by a digital toggle between two (or more) signal levels. This figure illustrates the different patterns that RTN has been observed to exhibit. While the magnitude and frequency of the toggle varies between pixels, the noise is consistent for a given pixel from integration to integration. RTN is thought to arise from single-electron trapping effects in the ROIC.

(a) Raw Data   (b) Dark Subtraction

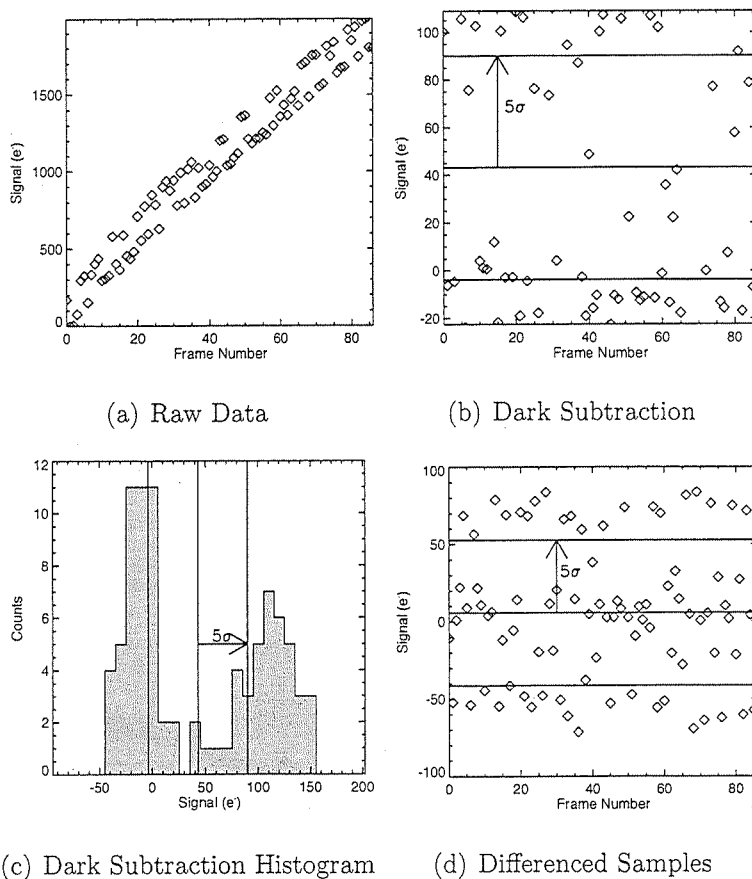(c) Dark Subtraction Histogram   (d) Differenced Samples

Fig. 9.— This figure illustrates the algorithm we have developed to locate pixels that exhibit RTN, such as the one shown in 9(a). The algorithm consists of a two step process. First, we identify noisy pixels, which we define to have samples beyond $\pm 5\sigma_{avg}$, where σ_{avg} is the average scatter in the ramps. To remove any offsets and correlated noise effects, a median dark is subtracted from the individual integration 9(b). For RTN pixels, two distinct states are apparent by visual inspection, but can be more clearly identified by the histogram in 9(c). To differentiate between RTN and other noise effects, we then difference successive data samples in order to identify the digital toggle associated with the two (or more) states 9(d). Again, a similar $\pm 5\sigma_{avg}$ threshold is used. The $5\sigma_{avg}$ threshold was chosen in order to best isolate RTN from other noise effects. Therefore, this algorithm provides a lower limit on the number of RTN pixels.
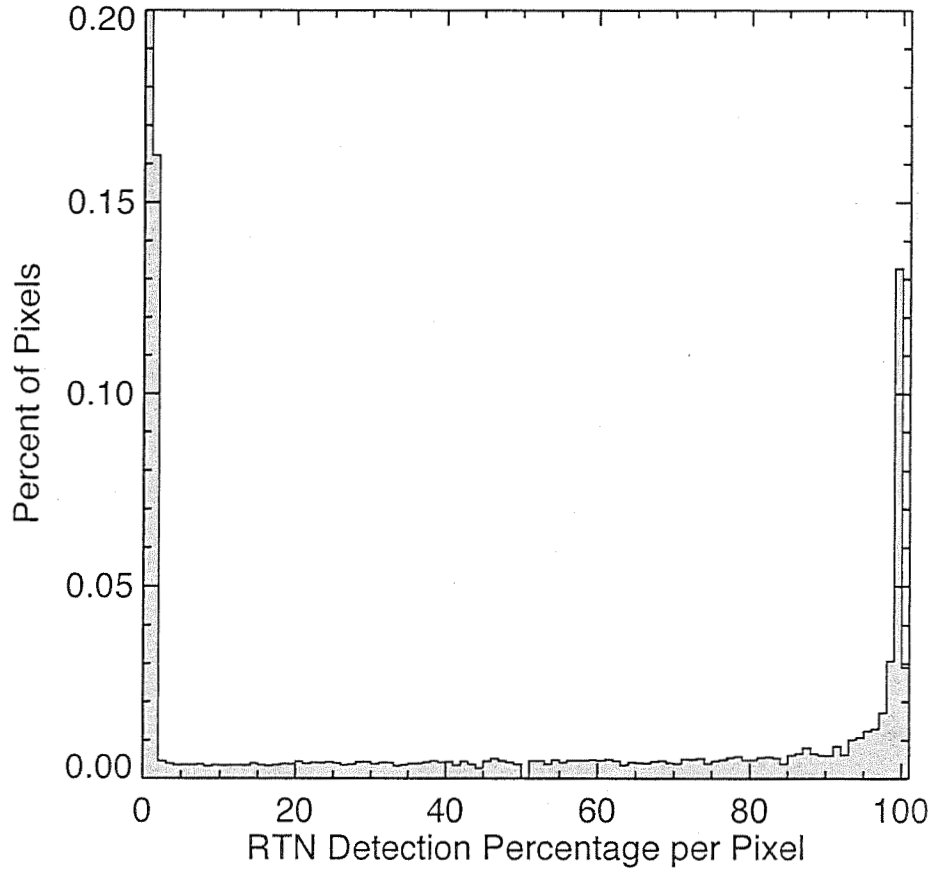
Fig. 10.— This histogram illustrates that RTN is largely confined to a small and fixed subset of pixels, making it a feature that can be tracked using operable pixel masks. The peak at bin 0, which extends to nearly 100%, indicates that the vast majority of pixels have no detectable RTN in any integration. The peak at bin 99 indicates that of pixels having detectable RTN in one integration, a majority have detectable RTN in almost every other integration. The noticeable peak at bin 1 and the drop off at bin 100, are due to the fluctuation in the magnitude of the RTN scatter above and below the set thresholds. The peak at bin 1 can also be partially attributed to the algorithm's <1% false detection rate.